The boundary data immersion method for compressible flows with application to aeroacoustics

Stefan C. Schlanderer[a,1,*], Gabriel D. Weymouth[a,2], Richard D. Sandberg[b,3]

[a]*Faculty for Engineering and the Environment*
University of Southampton, SO17 1BJ Southampton, United Kingdom
[b]*Department of Mechanical Engineering,*
University of Melbourne, Melbourne VIC 3010, Australia

Abstract

This paper introduces a virtual boundary method for compressible viscous fluid flow that is capable of accurately representing moving bodies in flow and aeroacoustic simulations. The method is the compressible extension of the boundary data immersion method (BDIM, Maertens & Weymouth (2015)). The BDIM equations for the compressible Navier-Stokes equations are derived and the accuracy of the method for the hydrodynamic representation of solid bodies is demonstrated with challenging test cases, including a fully turbulent boundary layer flow and a supersonic instability wave. In addition we show that the compressible BDIM is able to accurately represent noise radiation from moving bodies and flow induced noise generation without any penalty in allowable time step.

Keywords: boundary data immersion, immersed boundary method, aeroacoustics, compressible fluid flow, flow induced noise, noise from moving bodies

1. Introduction

Accurate computation of fluid flows in the vicinity of moving bodies with high accuracy is a severe challenge. Immersed boundary methods (IMBM)

*Corresponding author
[1]Present address: stefan.schlanderer@unimelb.edu.au
[2]G.D.Weymouth@soton.ac.uk
[3]richard.sandberg@unimelb.edu.au

have become a popular tool to impose boundary conditions upon boundaries that do not coincide with the computational grid (refer to [1] for a review). Besides the ability to simulate moving bodies this class of boundary methods enables the simulation of complex geometries on relatively simple meshes, thus reducing the effort of grid generation. Alongside with the enormous growth of computational power in recent years IMBMs have enabled the consideration of multi-physics phenomena such as fluid-structure interaction problems. Furthermore flow control and optimization problems incorporating moving control surfaces or morphing bodies can be studied with recent advances of IMBMs.

However, IMBMs often have a low order of accuracy or add significant computational overhead when used for moving bodies, where the IMBM needs to be reinitialized for each timestep. Additionally, sharp interface IMBMs have shown to produce non-physical pressure oscillations due to the so-called "freshly cleared" cell problem [2] which needs additional treatment as proposed in [3], [4], [5], [6] and [7]. This increases the complexity and computational cost of the method. These pressure oscillations were reduced significantly by the direct momentum forcing method proposed by Uhlman [8] where the boundary is not reconstructed but represented by volume forces that are evaluated on the boundary and then spread to surrounding grid points which leads to a smooth representation of the boundary. This method was later generalized to be used with arbitrarily shaped bodies [9] and Cartesian and curvilinear grids [10].

Many engineering applications are characterized by flows with high Reynolds numbers. However, a key problem with smooth IMBMs is the accurate prediction of intermediate to high Reynolds number flows. The reason for this weakness is a lack of accuracy of the representation of the velocity gradient at the wall. Considering a flat plate boundary layer the streamwise velocity component along the wall normal direction is continuous. This is ensured by the no-slip condition that is usually applied by setting the velocity of the fluid on the wall equal to the wall velocity, which is the principle of all IMBMs. In contrast to the velocity field itself, its gradient has a discontinuity in that direction at the interface between the fluid and solid domains, caused by the "kink" in the velocity profile. As the wall velocity gradient increases with Reynolds number this discontinuity becomes more significant [11]. Therefore the error made by momentum forcing approaches increases with an increase in Reynolds number. Furthermore force interpolation and spreading schemes used in momentum forcing approaches assume a smooth field otherwise they

become first order accurate or need additional treatment [12]. The higher error and lowered order of accuracy has to be compensated by a finer grid resolution. This typically goes along with a decrease in timestep when using explicit time integration schemes making such a strategy computationally prohibitively expensive.
The “Boundary Data Immersion Method”(BDIM) that has recently been proposed for incompressible simulations by Weymouth & Yue [13] and extended by Maertens & Weymouth [11] overcomes many of the aforementioned weaknesses. The concept of this approach is to map the governing equations of the solid body and fluid domain at the interface. This results in a set of meta equations that is valid in both domains and ensures a smooth transition. The smooth transition helps to avoid fresh cell treatment when moving bodies are considered. Maertens & Weymouth [11] increased the accuracy of the mapping between both domains by taking the normal derivative to the surface into account which improves the representation of the jump in the velocity gradient at the wall significantly.

The majority of previously published IMBMs and their extensions considered incompressible fluid flow. For aeroacoustics and compressible fluid flow there are only few methods published, among them are two for inviscid flow [14, 15]. In the class of noise propagation problems with prescribed noise sources Casalino et al.[16] and Arina [17] as well as Cand et al. [18] and Liu & Wu [19] presented IMBMs in the frequency and time domain, respectively. Hybrid approaches for aeroacoustic research obtain a noise source field from a flow simulation which is then used as input for acoustic analogies to calculate the acoustic far-field. For this class of computational aeroacoustics Seo & Mittal [20] developed a sharp interface IMBM for the linearized perturbed compressible equations (LPCE). They validated the method with flow induced noise from stationary objects and acoustic scattering problems. Another hybrid approach was employed by Margnat [21] who coupled an incompressible flow solver employing Goldstein’s feedback forcing [22] approach with Curle’s analogy.
To the authors knowledge all IMBM in the literature for viscous compressible flows were intended and validated to represent stationary bodies [23, 24, 25, 26, 27, 28]. Among these studies that consider aeroacoustics Sandberg & Jones [27] used a ghost cell approach to represent stationary flat plate extensions of airfoils to investigate trailing-edge noise with direct numerical simulations (DNS). Due to the complexity of the boundary reconstruc-

tion and the additional treatment for freshly cleared grid points this method would increase computational cost critically for moving boundary problems, rendering it unsuitable for high-fidelity. In the class of continuous forcing methods Liu & Vasilyev [26] developed a Brinkmann penalization method with a unique density treatment modelling the solid as a high impedance medium for aeroacoustic simulations, however without presenting results for flow induced noise. The feedback forcing character of this approach leads to timestep restrictions when using explicit time marching which increases computational cost prohibitively.
Thus, when using a compressible flow solver to directly compute the hydrodynamic and aeroacoustic field simultaneously a method is required that can include the effects of moving bodies and the associated noise generation. Such a method would also enable the consideration of vibro-acoustic problems. To that end the BDIM for the compressible Navier-Stokes equations is derived in this paper in section 2. The accuracy of the newly developed method is evaluated in section 3 with a focus on the representation of the flow around a cylinder (subsection 3.1) as well as turbulent (subsection 3.2) and supersonic (subsection 3.4) flat plate boundary layers. Section 4 validates the compressible BDIM for the use in aeroacoustic DNS demonstrating its capabilities for problems involving noise generation from moving (subsection 4.1) and stationary objects (subsection 4.2).

2. Derivation of the compressible flow boundary data immersion equations

In the following section 2.1 the concept of the BDIM as introduced in [13] and [11] is first revisted. Section 2.2 presents the derivation of the BDIM for the compressible Navier–Stokes equations. Finally the numerical methods of the code into which the compressible BDIM approach was implemented are briefly introduced in section 2.3.

2.1. The boundary data immersion method revisited

For the derivation of the BDIM meta equation a domain that incorporates a solid body subdomain Ω_s and a compressible fluid subdomain Ω_f are considered, as sketched in Figure 1. The general formulation for a meta

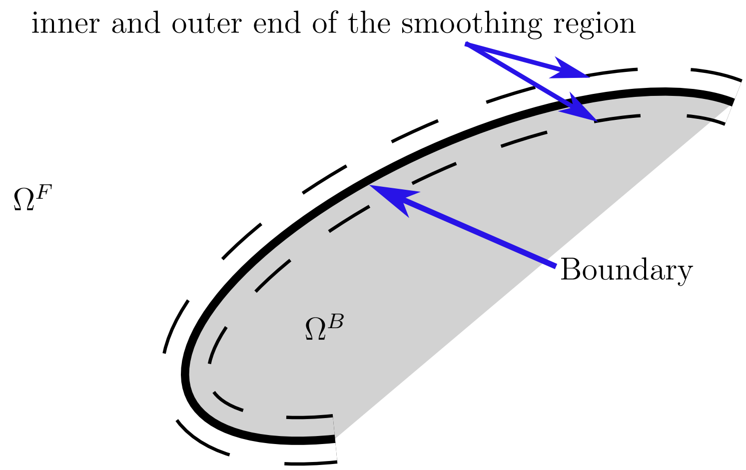

Figure 1: Subdomains under consideration for the derivation of the BDIM equations.

equation of an arbitrary field variable Φ is given by

$$\Phi_M(\vec{x},t) = \begin{cases} \Phi = b & \text{, for } \vec{x} \in \Omega_b \\ \Phi = f & \text{, for } \vec{x} \in \Omega_f \end{cases} \quad . \tag{1}$$

Both subdomains can then be smoothly coupled by a convolution of each governing equation with a nascent delta kernel K_ϵ of radius ϵ which results in

$$b_\epsilon(\Phi,\vec{x},t) = \int_{\Omega_b} b(\Phi,\vec{x}_b,t) K_\epsilon(\vec{x},\vec{x}_b)\mathrm{d}\vec{x}_b \qquad \text{and} \tag{2a}$$

$$f_\epsilon(\Phi,\vec{x},t) = \int_{\Omega_f} f(\Phi,\vec{x}_f,t) K_\epsilon(\vec{x},\vec{x}_f)\mathrm{d}\vec{x}_f \qquad , \tag{2b}$$

respectively. With this step the domain of each individual governing equation is extended to the whole domain which is the union of both subdomains $\Omega = \Omega_b \cup \Omega_f$. Hence the governing equation of the field variable Φ is simply

$$\Phi_\epsilon = b_\epsilon + f_\epsilon \qquad \text{for } \vec{x} \in \Omega \qquad . \tag{3}$$

The role of the convolution is to “switch off” the governing equations in the complementary subdomain where they are not valid (i.e. fluid equations in solid domain and vice versa). Furthermore it allows a smooth transition between both subdomains over a smoothing region with a half-width of ϵ, where both governing equations contribute to the overall solution. For a simplification of the convolution integrals two requirements are necessary:

1. smoothing only occurs near the boundary/interface
2. smoothing occurs in the normal but not in the tangential direction of the boundary.

Maertens and Weymouth [11] use a Taylor series expansion of the convolution integral and the two aforementioned requirements to derive simplified equations for both extended subdomain equations resulting in

$$b_\epsilon(\Phi,\vec{x},t) \approx b(\Phi,\vec{x},t)\,\mu_0^{\epsilon,B} + \frac{\partial b}{\partial n}(\Phi,\vec{x},t)\,\mu_1^{\epsilon,B} \qquad \text{and} \tag{4a}$$

$$f_\epsilon(\Phi,\vec{x},t) \approx f(\Phi,\vec{x},t)\,\mu_0^{\epsilon,F} + \frac{\partial f}{\partial n}(\Phi,\vec{x},t)\,\mu_1^{\epsilon,F} \qquad , \tag{4b}$$

with μ_0^ϵ being the zeroth and μ_1^ϵ first moments of the kernel ϕ_ϵ over their respective subdomains. Higher order terms are neglected as they would incorporate terms that are non-local and therefore violate requirement (1). Maertens and Weymouth [11] suggest to use the following kernel

$$\Phi_\epsilon(x,y) = \begin{cases} \frac{1}{2\epsilon}\left[1+\cos(\frac{|x-y|\pi}{\epsilon})\right] & \text{, for } |x-y|<\epsilon \\ 0 & \text{, for } |x-y|\geq\epsilon \end{cases} \tag{5a}$$

which results in the zeroth

$$\mu_0^{\epsilon,F}(d) = \begin{cases} \frac{1}{2}\left[1+\frac{d}{\epsilon}+\frac{1}{\pi}\sin(\frac{d}{\epsilon}\pi)\right] & \text{, for } |d|<\epsilon \\ 0 & \text{, for } d\leq-\epsilon \\ 1 & \text{, for } d\geq\epsilon \end{cases} \qquad \text{and first} \tag{6a}$$

$$\mu_1^{\epsilon,F}(d) = \begin{cases} \epsilon\left[\frac{1}{4}\left(1-\frac{d}{\epsilon}^2\right)-\frac{1}{2\pi}\left(\frac{d}{\epsilon}\sin(\frac{d}{\epsilon}\pi)+\frac{1}{\pi}\left(1+\cos(\frac{d}{\epsilon}\pi)\right)\right)\right] & \text{, for } |d|<\epsilon \\ 0 & \text{, for } |d|\geq\epsilon \end{cases} \tag{6b}$$

moment of the kernel 5, respectively, and are visualized in figure 2. In these expressions for the zeroth and first kernel moment, d is the signed distance from the surface where values with $d<0$ refer to the inside and $d>0$ to the

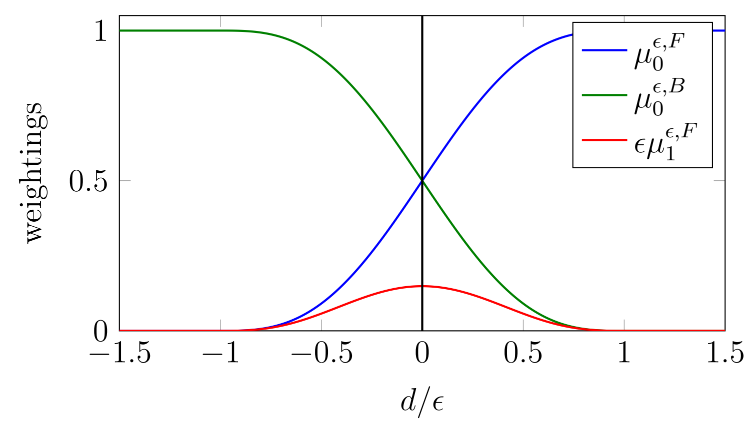

Figure 2: Zeroth and first moment of the kernel for the fluid and solid body domain in the vicinity of the wall surface.

outside of the solid body. For the solid body domain the symmetry of the kernel functions can be used resulting in $\mu_0^{\epsilon,B}(d) = \mu_0^{\epsilon,F}(-d) = 1 - \mu_0^{\epsilon,F}(d)$ and $\mu_1^{\epsilon,B}(d) = \mu_1^{\epsilon,F}(-d) = -\mu_1^{\epsilon,F}(d)$, respectively [11]. Using equation 3 with 4 and the kernel moments from equation 6 the resulting meta equation can be assembled and results in

$$\begin{aligned} \Phi_\epsilon = {} & f(\Phi, \vec{x}, t)\, \mu_0^\epsilon + b(\Phi, \vec{x}, t)\ (1 - \mu_0^\epsilon) \\ & + \mu_1^\epsilon \frac{\partial}{\partial n} \left(f(\Phi, \vec{x}, t) - b(\Phi, \vec{x}, t) \right) \qquad . \end{aligned} \tag{7}$$

This meta equation will be used in the following section to derive the BDIM equations for compressible flows. Furthermore we will denote results "first order" when we do not include the derivative correction in equation 7, hence $\mu_1^\epsilon = 0$. The framework will be called second order when the derivative term is included.

In the vicinity of sharp edges of a body surface, e.g. a rectangular trailing-edge, the kernel moments need to be interpolated between two line segments in order to properly account for the contribution of both surfaces. To that end we use the interpolation approach detailed in AppendixA.

2.2. The Boundary Data Immersion Method for the Compressible Navier-Stokes Equations

In order to use the BDIM meta equation in a compressible flow solver, the compressible Navier-Stokes equations governing the fluid need to be mapped to the governing equation of the solid body. The non-dimensional conservative fluid equations in tensor notation can be expressed with

$$\frac{\partial \rho}{\partial t} + \frac{\partial}{\partial x_k}(\rho u_k) = 0 \ , \tag{8a}$$

$$\frac{\partial}{\partial t}(\rho u_i) + \frac{\partial}{\partial x_k}(\rho u_i u_k) = -\frac{\partial p}{\partial x_k}\delta_{ik} + \frac{\partial}{\partial x_k}\tau_{ik} \ , \tag{8b}$$

$$\frac{\partial}{\partial t}(\rho E) + \frac{\partial}{\partial x_k}(\rho u_k E) = \frac{\partial}{\partial x_k}\left[u_i \tau_{ik} - u_k p - q_k\right] \ . \tag{8c}$$

In this set of equations the conservation of mass is expressed by 8a, conservation of momentum by 8b and finally conservation of total energy(ρE) by 8c. The fluid velocity is denoted by u_i, density by ρ, static pressure by p and the temperature by T. The total energy E is defined as $E = T/\left[\gamma(\gamma-1)M^2\right] + 1/2 u_i u_i$ and the stress tensor and heat-flux vector are computed as

$$\tau_{ik} = \frac{\mu}{Re}\left(\frac{\partial u_i}{\partial x_k} + \frac{\partial u_k}{\partial x_i} - \frac{2}{3}\frac{\partial u_k}{\partial x_k}\delta_{ik}\right) \quad \text{and} \quad q_k = \frac{-\mu}{(\gamma-1)M^2 Pr Re}\frac{\partial T}{\partial x_k} \ , \tag{9}$$

respectively, where M is the Mach number, Re the Reynolds number and Pr the Prandtl number which is assumed to be constant at $Pr = 0.72$. The Mach and Reynolds numbers are a result of the non-dimensionalization. Finally the system of equations is closed by obtaining the pressure p with the non-dimensional equation of state $p = (\rho T)/(\gamma M^2)$ where $\gamma = 1.4$ is the isentropic exponent of air.

For the introduction of the governing equation of the solid body the dependence of all quantities on the location is neglected in the notation throughout the following paragraphs. Nevertheless all quantities can vary in space. The conservation of mass for a solid results in the same expression as for a compressible fluid, namely

$$\frac{\partial \rho}{\partial t} + \frac{\partial}{\partial x_k}(\rho u_k) = 0 \qquad . \tag{10}$$

Furthermore the solid body has a prescribed velocity $V(\vec{x}, t)$ which can be provided a priori with an analytical equation or a time dependent solution from a structural solver or a flow control framework. In addition the temperature T_s within the solid body domain is prescribed as a constant or by another input function. Hence the governing equation for the velocity b_V and temperature b_T of the solid body are

$$b_{V_i} = u_{i,b}(t) = V_{s,i}(t) \qquad \text{and} \tag{11a}$$

$$b_T = T_b(t) = T_s(t) \qquad . \tag{11b}$$

Since the conservation of mass exploits the same physical principle and has the same expression in both subdomains no mapping of the governing equations is needed.

Before the velocity equation 11a of the solid can be mapped to the momentum equation 8b of the fluid, both equations need to be reformulated in order to describe the same physical quantities. The left-hand side of equation 8b can be expanded as

$$\begin{aligned} \frac{\partial}{\partial t}(\rho u_i) + \frac{\partial}{\partial x_k}(\rho u_i u_k) &= u_i \frac{\partial \rho}{\partial t} + \rho \frac{\partial u_i}{\partial t} + \rho u_k \frac{\partial u_i}{\partial x_k} + u_i \frac{\partial \rho u_k}{\partial x_k} \\ &= \rho \left[\frac{\partial u_i}{\partial t} + u_k \frac{\partial u_i}{\partial x_k} \right] \qquad . \end{aligned} \tag{12}$$

The sum of the first and the last term of right-hand-side of the expanded equation are the continuity equation multiplied by u_i and therefore are zero. Hence, after some rearrangement with the right-hand side from equation 8b the change of the fluid velocity in time is

$$\frac{\partial u_i}{\partial t} = -u_k \frac{\partial u_i}{\partial x_k} + \frac{1}{\rho} \left[-\frac{\partial p}{\partial x_k} \delta_{ij} + \frac{\partial}{\partial x_k} \tau_{ij} \right] = RHS_{u,i} \qquad . \tag{13}$$

$RHS_{u,i}$ will be used as an abbreviation for the right-hand-side of the velocity equation in the following derivation. The expression for the velocity field can then be obtained by integrating this equation over a time step Δt resulting in

$$f_v(u_i, t_0 + \Delta t) = u_{i,f}(t_0 + \Delta t) = u_{i,f}(t_0) + \int_{t_0}^{t_0 + \Delta t} RHS_{u,i} \, dt \qquad . \tag{14}$$

With an Euler forward integration or a generalized Runge-Kutta substep in time this equation can be discretized with

$$f_v(u_i, t_0 + \Delta t) = u_{i,f}(t_0 + \Delta t) = u_{i,f}(t_0) + RHS_{u,i}\,\Delta t \qquad . \tag{15}$$

Since the governing equations for the velocity in both subdomains are now defined with equation 11a and 15 they can be replaced in 7 which leads to

$$\begin{aligned} u_{i,\epsilon}(t_0 + \Delta t) = {} & \left[u_{i,f}(t_0) + RHS_{u,i}\Delta t\right] \mu_0^\epsilon \; + \; V_i(t)\,(1 - \mu_0^\epsilon) \\ & + \; \mu_1^\epsilon \frac{\partial}{\partial n} \left[u_{i,f}(t_0) + RHS_{u,i} - V_i(t)\right] . \end{aligned} \tag{16}$$

In contrast to incompressible fluid solvers where the pressure equation is commonly solved separately from the rest of the right hand side of equation 13, all of these terms are commonly treated equally in compressible frameworks. Therefore the mapped velocity field of the fluid can be summarized with its integral formulation which results in

$$u_{i,\epsilon}(t) = u_{i,f}(t)\mu_0^\epsilon \; + \; V_i(t)\,(1 - \mu_0^\epsilon) \; + \; \mu_1^\epsilon \frac{\partial}{\partial n} \left[u_{i,f}(t) - V_i(t)\right] \qquad . \tag{17}$$

Following the same approach as for the velocity equation the left hand side of the total energy equation 8c can be expanded as

$$\frac{\partial}{\partial t}(\rho E) + \frac{\partial}{\partial x_k}(\rho u_k E) = E\frac{\partial \rho}{\partial t} + \rho \frac{\partial E}{\partial t} + \rho u_k \frac{\partial E}{\partial x_k} + E\frac{\partial \rho u_k}{\partial x_k} \qquad . \tag{18}$$

The sum of the first and the last terms of the right-hand-side of the expanded equation are the continuity equation multiplied by the total energy E and hence add up to zero. By substituting the definition of the total energy $E = T/\left[\gamma(\gamma-1)M^2\right] + 1/2 u_i u_i$ and using the abbreviation $T/\left[\gamma(\gamma-1)M^2\right] = \chi$ this yields

$$\begin{aligned} \rho\frac{\partial E}{\partial t} + \frac{\partial}{\partial x_k}(\rho u_k E) &= \rho\left[\chi\frac{\partial T}{\partial t} + \frac{1}{2}\frac{\partial u_i u_i}{\partial t}\right] + \rho u_k \left[\rho\chi\frac{\partial T}{\partial x_k} + \frac{1}{2}\frac{\partial u_i u_i}{\partial x_k}\right] \\ &= \rho\left[\chi\frac{\partial T}{\partial t} + u_i\frac{\partial u_i}{\partial t}\right] + \rho u_k \left[\chi\frac{\partial T}{\partial x_k} + u_i\frac{\partial u_i}{\partial x_k}\right] \\ &= \rho\left[\chi\frac{\partial T}{\partial t} + u_k\chi\frac{\partial T}{\partial x_k}\right] + \rho u_i \left[\frac{\partial u_i}{\partial t} + u_k\frac{\partial u_i}{\partial x_k}\right] \qquad . \end{aligned} \tag{19}$$

The two terms in the final brackets of the last line are the left hand side of the expanded momentum equation 12 multiplied by u_i. They represent the change of kinetic energy of the fluid after applying the chain rule. Using that fact together with the right hand side of equation 8c, the change of temperature in time can be expressed by

$$\begin{aligned}\frac{\partial T}{\partial t} &= -u_k \frac{\partial T}{\partial x_k} + \frac{1}{\rho\chi}\frac{\partial}{\partial x_k}\left[u_i \tau_{ik} - u_k p - q_k + u_i p \delta_{ik} - u_i \tau_{ik}\right] \\ &= -u_k \frac{\partial T}{\partial x_k} + \frac{1}{\rho\chi}\frac{\partial}{\partial x_k}\left[-u_k p - q_k + u_i p \delta_{ik}\right] = RHS_T \qquad .\end{aligned} \tag{20}$$

Analogous to the time integration of the velocity field the temperature at time $t = t_o + \Delta t$ is

$$f_T(T, t_0 + \Delta t) = T_f(t_0 + \Delta t) = T_f(t_0) + RHS_T\, \Delta t \tag{21}$$

and can be substituted into the general meta equation together with the governing equation for the solid's temperature 11b

$$\begin{aligned}T_\epsilon(t_0 + \Delta t) = &\left[T_f(t_0) + RHS_T \Delta t\right] \mu_0^\epsilon + T_s(t)\left(1 - \mu_0^\epsilon\right) \\ &+ \mu_1^\epsilon \frac{\partial}{\partial n}\left[T_f(t_0) + RHS_T \Delta t - T_s(t)\right] .\end{aligned} \tag{22}$$

With the same reasoning that was used for the velocity field the BDIM equation for temperature can be simplified with its integral formulation

$$T_\epsilon(t_0 + \Delta t) = T_f(t)\mu_0^\epsilon + T_s(t)\left(1 - \mu_0^\epsilon\right) + \mu_1^\epsilon \frac{\partial}{\partial n}\left[T_f(t) - T_s(t)\right] \qquad . \tag{23}$$

As the resulting BDIM equations can all be expressed with the integral formulation the boundary data immersion method can be applied after the time integration and no adaptation of the original time-stepping algorithm for the right hand side is needed. Furthermore this is consistent with the application of body-fitted boundary conditions which are commonly performed at the same stage of the simulation.
A comparison between the derived meta equations 17 and 23 and discrete momentum forcing reveals that the first order BDIM is very similar to discrete momentum forcing. When the μ_0^ϵ and $1 - \mu_0^\epsilon$ terms are regarded as the interpolation and force spreading operators, then the only difference between both approaches is the physical reasoning for using them and how these op-

erators work. The analytical and general reasoning, however, is a strength of the BDIM approach, offering robust and smooth coupling where other approaches such as discrete momentum forcing need additional treatment for moving bodies. In addition the second order extension of the approach offers higher order interpolation between both subdomains and reduces bias of the velocity gradient discontinuity.

In the incompressible meta equations derived in [13] and [11] there is an additional weighting for the pressure term as a boundary condition for the pressure equation. This is a result of the special algorithmic treatment of the pressure by the Poisson equation in incompressible flow simulations, which is in principle not required in the present compressible framework. However, it was found that for bluff bodies where the body surface alignment with the underlying grid is arbitrary, instabilities on single grid points could grow just inside the smoothing region. These instabilities would eventually lead to diverging simulations. Analysis of the contributing terms of the continuity equation

$$\frac{\partial \rho}{\partial t} = -\frac{\partial}{\partial x_k}\left(\rho u_k\right) = -\left(\rho \frac{\partial u_k}{\partial x_k} + u_k \frac{\partial \rho}{\partial x_k}\right) \tag{24}$$

at these grid points showed that the instabilities were caused by the bias in the derivative terms of the velocity, i.e. the first term which contains the incompressible contribution. In particular the derivative in the wall tangential direction lead on average to a non-zero right-hand side of the continuity equation. In order to ensure robust simulations without prescribing something unphysical it is suggested to map the right hand side of equation 24 to

$$\frac{\partial \rho}{\partial t} = -\left(\rho \frac{\partial u_n}{\partial n}\right) \quad . \tag{25}$$

Here the subscript and direction n mean the wall normal direction. This is exactly the simplified right hand side of the continuity equation at the wall for a stationary body. In this case the second term of equation 24 is zero and the only non-zero component of the first term is the one in the wall normal direction. Strictly speaking equation 25 is not the governing equation of the solid interior but an interface condition. Replacing equation 24 and 25 in the general meta equation 7 results in

$$\frac{\partial \rho_\epsilon}{\partial t} = -\frac{\partial\left(\rho u_k\right)}{\partial x_k}\mu_0^\epsilon - \left(\rho\frac{\partial u_n}{\partial n}\right)\left(1-\mu_0^\epsilon\right) - \mu_1^\epsilon \frac{\partial}{\partial n}\left(\frac{\partial\left(\rho u_k\right)}{\partial x_k} - \left(\rho\frac{\partial u_n}{\partial n}\right)\right) \tag{26}$$

as meta equation for the right-hand of the continuity equation.

2.3. Numerical methods to solve the compressible Navier-Stokes equations

The code that was used to validate the compressible BDIM solves the Navier–Stokes equations employing a 4^{th}-order accurate standard-difference scheme with Carpenter boundary stencils [29] to calculate derivatives. The scheme can be applied to general geometries by pre-multiplication of metric terms. Time marching is achieved employing an ultra low-storage five-step 4^{th}-order accurate Runge–Kutta scheme [30]. The stability of the code is enhanced by a skew-symmetric splitting of the nonlinear terms [31]. Furthermore a sixth-order accurate high-wavenumber cut-off filter [32] with a weighting of $0.1 - 0.2$ is employed after every full Runge–Kutta cycle. Unphysical numerical reflections at the domain boundaries are avoided by using characteristic boundary conditions. At the inflow they are applied in an integral formulation as described by Jones [33]. For the outflow a zonal characteristic boundary condition [34] is used to avoid spurious pressure-oscillations from the outflow boundary which is subject to the passage vortical structures.

3. Validation for hydrodynamic accuracy

3.1. Flow around cylinder

The canonical flow around a static cylinder at Reynolds number $Re_{D_{cyl}} = 100$ is considered first as a validation case which offers a large number of reference data in the literature. The Mach number was set to $M = 0.1$, thus compressibility effects are expected to be negligible. The flow is simulated in a domain where the cylinder is placed at the origin and the domain boundaries are $-27D_{cyl} < x < 30D_{cyl}$ and $-30D_{cyl} < y < 30D_{cyl}$. The cylinder is immersed in a fluid flow with a streamwise velocity of unity which is prescribed at the inflow. The upper and lower boundaries are modelled as non-reflective characteristic freestream boundary conditions. At the outflow boundary the zonal characteristic boundary condition proposed in [34] is employed. The grid is spaced uniformly in the x and y directions within and a region of $-2R_{cyl} < x < 2R_{cyl}$ and $-2R_{cyl} < y < 2R_{cyl}$. The uniform grid spacing was $\Delta x = D_{cyl}/120$, thus resulting in 180 points within the equidistant discretization. The grid was then stretched towards the boundaries over 95 grid points with polynomial functions. The smoothing region half-width is set to $\epsilon = 2\Delta x = 2\Delta y$. The mapping of the continuity equation as introduced in equation 26 is employed in that case.

Source	St	C_D	C_L	C_{Dp}	C_{Df}	C_{Lp}	C_{Lf}
Exp.	0.164	1.25	-	-	-	-	-
[35]	0.165	1.33 ± 0.009	± 0.3321	0.99 ± 0.0082	± 0.0010	± 0.295	± 0.042
[36]		1.33		1.00	0.32	-	-
[37]	0.172	1.42	± 0.3536	-	-	-	-
[38]	0.164	1.34 ± 0.011	± 0.315	-	-	-	-
[39]	0.167	1.35 ± 0.012	± 0.315	-	-	-	-
[40]	0.165	1.34 ± 0.007	± 0.276	-	-	-	-
[11]1st order	0.167	1.31 ± 0.009	± 0.321	1.01 ± 0.0085	0.30 ± 0.0008	± 0.292	± 0.035
[11]2nd order	0.167	1.31 ± 0.009	± 0.313	1.00 ± 0.0081	0.30 ± 0.0007	± 0.285	± 0.034
1st order	0.165	1.35 ± 0.011	± 0.348	1.03 ± 0.0104	0.32 ± 0.0010	± 0.314	± 0.040
2nd order	0.165	1.32 ± 0.001	± 0.333	1.02 ± 0.0010	0.30 ± 0.0008	[illegible]	± 0.036

Table 1: Summary of the results from the cylinder case employing the first and second order BDIM to represent the cylinder shape for the baseline resolution of $\Delta x = D_{cyl}/120$. The results are compared to experimental data (St from [41] with estimated uncertainty of 0.8%, C_D from [42] with estimated measurement error of 6%), body-fitted simulations [35, 36, 37] and other IMBMs [38, 39, 40, 11].

3.1.1. Assessment of Accuracy

The forces acting on the cylinder are calculated from the pressure and skin-friction values on the surface of the cylinder. To that end the cylinder surface was discretized by 360 points equally distributed over the circumference. Since the values within the smoothing region are not physical the surface quantities were evaluated with a distance of ϵ. The accuracy of the pressure force is expected to not be affected by that. However, the skin-friction will be underestimated with this method. This is not a specific problem related to the BDIM but occurs in other IMBM approaches as well. The relevant flow quantities, i.e pressure and wall normal velocity gradient are interpolated from the four surrounding fluid grid points onto the surface grid using bilinear interpolation as described in [43].

The final values for the lift and drag are obtained by a panel integration over all surface points. The results for the Strouhal number, the lift fluctuations as well as the drag are presented in table 1. They are presented alongside data available in the literature from experiments [41, 42], body-fitted simulations [35, 36, 37] and other IMBMs [38, 39, 40, 11]. Given the scatter among the reported results the data obtained from simulations with the BDIM agree reasonably well with the values from literature.

3.1.2. *Formal order of convergence*

In order to evaluate the formal order of convergence for the numerical setup the simulation of the flow around the cylinder was repeated on six grids that were coarser than the one of the baseline simulation from the previous section. The resolution levels are defined in multiples n of the baseline resolution with $nD_{cyl}/120 = [3, 4, 6, 8, 10]$. The computational cost for the study was reduced by setting the Mach number to $M = 0.3$ which allowed an increase of the time step of the simulation. Since there is no analytical solution for this flow problem the data from the highly resolved case presented in the previous section with a grid spacing of $\Delta x = \Delta y = D_{cyl}/120$ was used as a reference.

Commonly the L_2 norm is considered as a measure for the global error ~~made by the boundary scheme~~. The L_∞ on the other hand highlights the local error close to the boundary. Figure 3 presents the results for the convergence study in the L_2 (3a and 3b) as well as in the L_∞ (3c and 3d) norm for the velocity and pressure fields over the different grid resolutions. In general it can be found that the results with the first order framework always yield an error that is higher than that obtained with the second order correction. For the L_2 and L_∞ norms the difference in error of the velocity field from the first order approach is a factor of $2.6 - 8.6$ higher than that of the second order BDIM. For the pressure field the differences are a bit lower but still significant with a factor of $2.0 - 3.0$. Each plot of figure 3 also shows first and second order slopes. Comparing these to the convergence data one can find that the first order approach yields a convergence rate that is slightly higher than first order for the velocity field (3a and 3c) in both the L_2 and L_∞ norm. In contrast to that the second order framework shows second order convergence approximately in the L_2 and L_∞ norm. For the pressure field the convergence rates of both approaches are approximately the same with second order for the higher resolution levels and slightly lower for the coarsest two.

3.2. *Turbulent Boundary layer*

In many engineering applications featuring fluid flow with moving or stationary solid objects the flow is turbulent. For IMBMs the main challenge in representing such flows is the high velocity gradient at the wall which increases with Reynolds number. As a result of that the discontinuity in the velocity gradient profile at the wall will grow as well. In particular aeroacoustic noise generation from the interaction of fluid flow with solid objects such

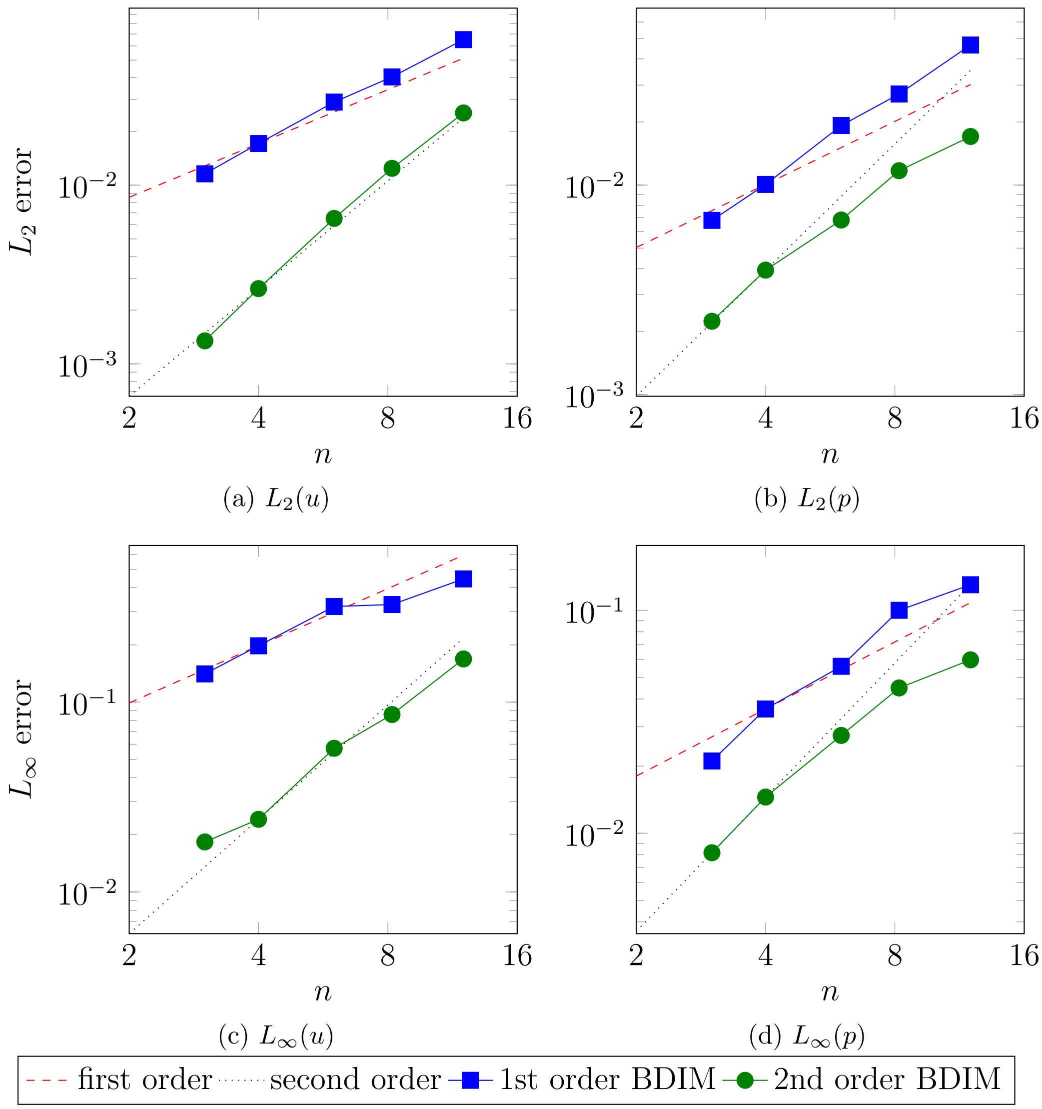

(a) $L_2(u)$ (b) $L_2(p)$ (c) $L_\infty(u)$ (d) $L_\infty(p)$

Figure 3: L_2 and L_∞ convergence of the velocity and pressure field for the flow around a stationary cylinder. A first and second order slope are shown as reference.

as turbulent interaction or trailing-edge noise is very sensitive to an accurate representation of the physics in the near wall region. The fully turbulent flow over a flat plate is used to assess the accuracy of the BDIM in representing the near wall physics in the presence of the relatively high velocity gradient discontinuity and to assess the BDIM's performance for problems featuring a large range of temporal and spatial scales.

3.2.1. Numerical Setup

The domain for the turbulent boundary layer incorporated the streamwise range of $1073 < Re_\theta < 1595$ where Re_θ is the Reynolds number based on momentum thickness. The wall normal grid spacing was constant along the streamwise direction. When scaled with the local viscous units the maximum spacing was $\Delta y^+ = 0.97$. In the wall normal direction the grid was stretched towards the freestream boundary over 90 grid points to $\Delta y^+ = 106$ at a distance of $20.6\delta^*$, where δ^* is the displacement thickness at the outflow. The grid spacing in the streamwise direction was uniform with maximum value of $\Delta x^+ = 18.0$ when scaled with the local viscous units. The spanwise domain width was $l_z = 5\delta^*$. A spectral method with 32 modes was used to discretize the domain width which yields a spanwise grid spacing of $\Delta z^+ = 8.13$. At the inflow synthetic turbulent fluctuations were superimposed to a mean turbulent velocity profile. To that end random fluctuations were filtered using the digital filter method proposed by Klein et al. [44] and extended to compressible flows by Touber & Sandham [45]. This method has been shown to result in good predictions of second order moments such as velocity fluctuations and integral turbulent length scales downstream of a development region with roughly 20δ length. The freestream and outflow boundary condition were both prescribed using characteristic boundary conditions. At the outflow the zonal approach was employed [34].
When the BDIM was employed to impose the wall boundary condition 20 grid points were mirrored below the actual surface of the wall and initialized with zero velocity, uniform density and the wall temperature.

3.3. Results

One of the main challenges for immersed boundary methods that do not modify the discretization at the boundary by reconstructing the boundary is posed through the discontinuity of the wall velocity gradient $\frac{\partial u_1}{\partial x_2}$. Figure 4 presents the streamwise velocity profile and its wall normal gradient in direct

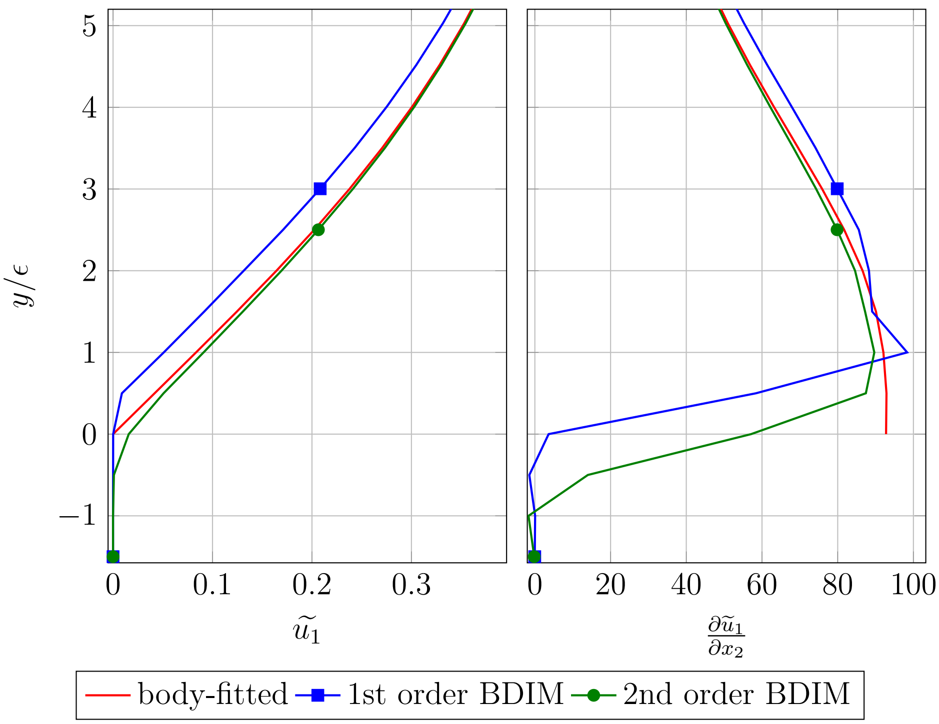

Figure 4: Streamwise velocity profile and its gradient in wall normal direction over the wall normal distances normalized by the smoothing region halfwidth ϵ in direct vicinity of the wall for the turbulent boundary layer flow at $Re_\theta \approx 1410$.

vicinity of the wall for the body-fitted and the two BDIM simulations. The kink and discontinuity in the velocity profile and its derivative, respectively, are immediately apparent in the body-fitted simulation. The results obtained with the first order BDIM show that the velocity profile is offset towards the free stream at all wall normal locations. Furthermore the smoothing region of halfwidth $\epsilon = 2\Delta y$ is hardly used to transition from the governing equations of the solid body to the fluid. In contrast, the second order BDIM features a much smoother transition between the two sets of governing equations and also takes advantage of a larger fraction of the smoothing region. In that case the deviation in the velocity profile from the body-fitted reference is very small at the boundary of the smoothing region and can be neglected at greater wall distances.

Considering the wall normal derivative of the velocity profile it can be found that the first order BDIM introduces overshoots towards the solid body and

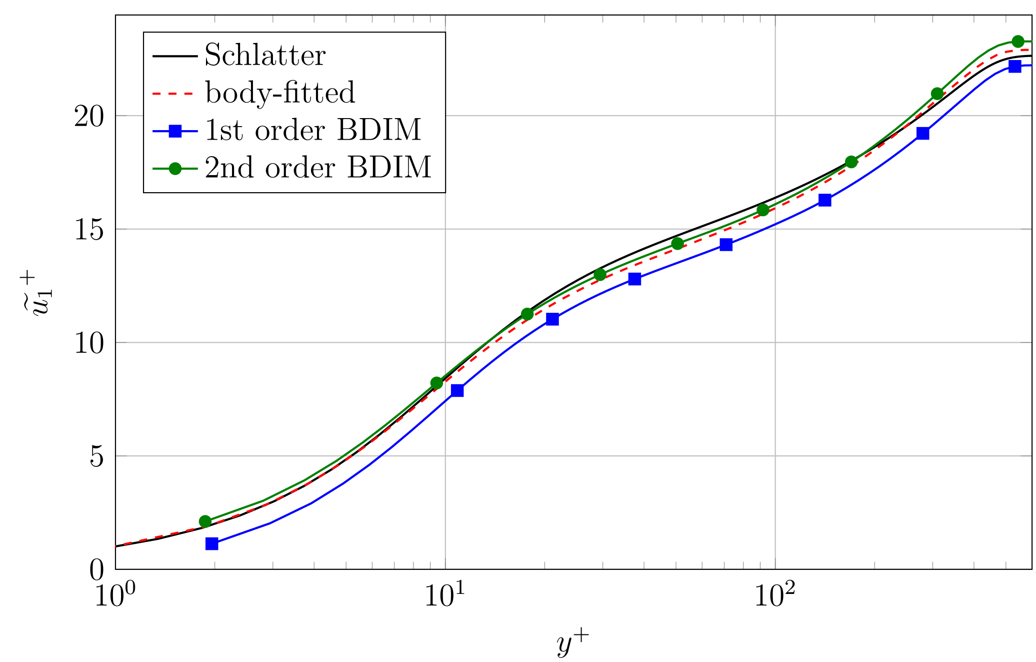

Figure 5: Turbulent boundary layer velocity profile scaled with viscous units comparing the BDIM to the body-fitted boundary conditions and the reference data from Schlatter and Örlü [46]. The normalization of the velocity profiles from the BDIM simulations was calculated with $\frac{\partial \widetilde{u_1}}{\partial x_2}$ at $y = \epsilon$.

the fluid. The maximum overshoot is at the fluid boundary of the smoothing region and significant deviations from the reference as well as an offset towards the freestream can be observed. When the second order correction is employed there is only a single overshoot towards the solid and the discontinuity is bridged in a considerably smoother fashion. The difference to the reference at the fluid boundary is fairly small and vanishes towards the freestream.

Turbulent quantities are commonly normalized by viscous scales derived from the friction velocity $u_\tau = \sqrt{\nu \frac{\partial \widetilde{u_1}}{\partial x_2}}$ for which the wall gradient $\frac{\partial \widetilde{u_1}}{\partial x_2}$ is needed. From the discussion of Figure 4 it is apparent that the value at the wall location will not yield any meaningful results when the BDIM is employed, which is a common difficulty for IMBMs. However, the value of $\frac{\partial \widetilde{u_1}}{\partial x_2}$ at the fluid boundary $y = \epsilon$ can be used as reasonable approximation for the value at the wall itself. Figure 5 compares the streamwise velocity profile scaled in viscous units from simulations obtained with our code and the incompressible reference data provided by Schlatter and Örlü [47]. It can be observed that the body fitted simulation shows slight deviations from the reference in the wake region. This can be attributed to the short domain and inflow length of the current case and the relatively low Reynolds number of $Re_\theta = 1410$. However, for the purpose of a comparison of the effect of different wall boundary conditions, i.e. body-fitted and immersed boundary the agreement is reasonable. The comparison of the first order BDIM with the data from the body-fitted case confirms the initial observation of an offset in Figure 4. The effect of this offset leads to considerable deviations from the reference far into the outer region due to the wrong scaling derived from $\frac{\partial \widetilde{u_1}}{\partial x_2}$. However, when the data is scaled with the velocity gradient from the body-fitted simulations the velocity profile matches the reference for $y^+ > 20$ but shows the same offset for $y^+ < 20$. In contrast to that the second order BDIM shows very good agreement throughout the entire profile with some minor overestimates. As for the first order framework the agreement of the case employing the second order correction with the reference is improving further when the profile is scaled by viscous units calculated from the body-fitted simulation.

Figure 6 presents Favre averaged velocity fluctuation profiles scaled in viscous units. The comparison of the body-fitted case and Schlatter's and Örlü's [47] data again shows some minor differences in particular for the streamwise component σ_{11}. This is due to the reasons noted earlier and for the sake of assessing the BDIM approach the agreement is seen as sufficiently good. The offset in the data obtained with the first order BDIM is prominent in all components and besides the offset all amplitudes are underestimated. The second order framework improves the offset considerably, as already seen for the velocity profile before. The shape of the profile as well as the amplitude is captured well for all components but the streamwise velocity fluctuations σ_{11} where the amplitude is overestimated. However, when the data obtained from both BDIM simulations is scaled with viscous units of the body-fitted case the deviation in the peak amplitude of the σ_{11} component vanishes and overall good agreement is obtained with the reference data.

Thus it can be concluded that the BDIM approach can be used to accurately represent a wall when wall bounded turbulence is considered. I~~t could be shown that t~~he second order correction improved the results considerably.

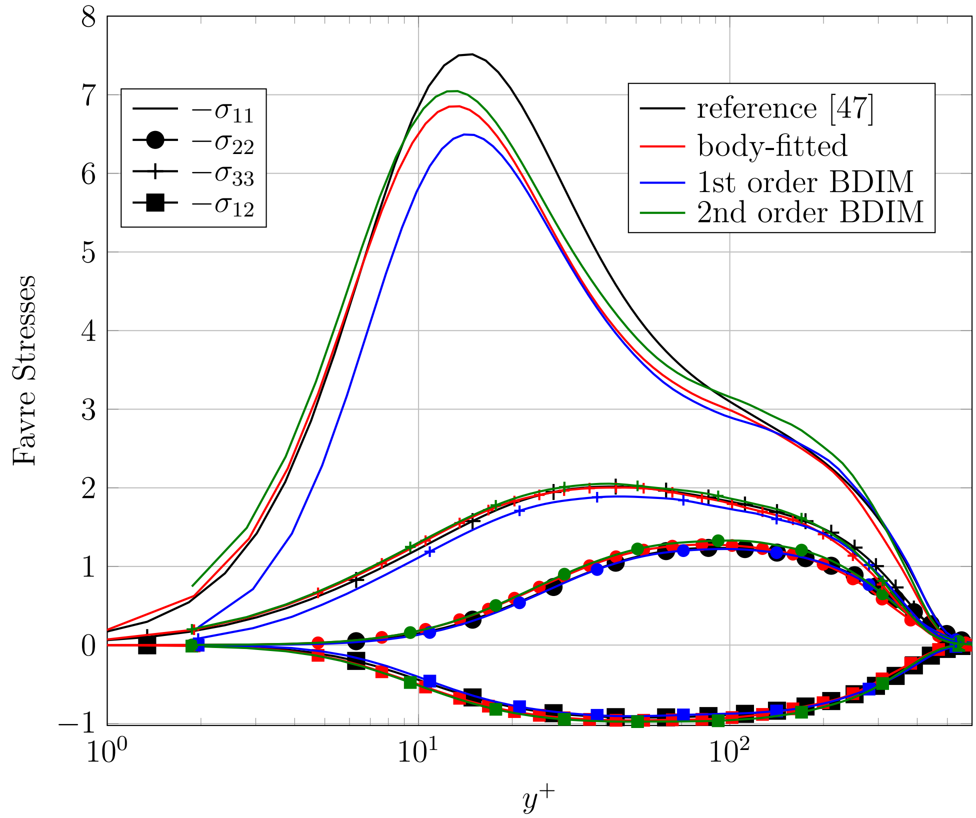

Figure 6: Turbulent boundary layer velocity fluctuations profiles scaled with viscous units comparing the BDIM to the body-fitted boundary conditions and reference data from literature [47]

This can be attributed to the much better representation of the discontinuity present in the velocity gradient at the wall.

3.4. Oblique wave growth in a supersonic boundary layer

When flow induced noise through fluid solid interaction is considered, a very accurate representation of the near-wall flow is crucial. This is attributed to the fact that fluctuations in the boundary layer are the "input" of the noise scattering mechanism. The growth of viscous instabilities, also denoted oblique waves, in a supersonic flat plate boundary layer at $M = 3$ is considered as a rigorous test case for the representation of the near-wall physics. This validation problem assesses the correct modelling of the thermodynamic fluctuations close to the wall in particular. In high-fidelity direct

noise computations this is an important aspect since the noise is calculated directly from the compressible Navier–Stokes equations.
Oblique waves are three dimensional instabilities that can lead to breakdown into turbulence in supersonic boundary layers. They are considered particularly relevant in low disturbance environments since they need very low disturbance thresholds to be initiated. The oblique breakdown features a linear, an early and a late non-linear regime [48]. For the validation of the BDIM the focus is on simulating the linear regime.

3.4.1. Numerical Setup

The flow under consideration is a supersonic flat plate boundary layer at $M = 3.0$ and $Re = 1,578,102$. In order to trigger the instabilities the flow was disturbed close to the wall by adding a forcing term to the right hand side of the wall normal momentum component in the second spanwise Fourier mode. The amplitude of the volume force was $A = 1.0 \times 10^{-3}$ and the frequency was $f = 12.558136$. The forcing was spread over a circular area in the $x - y-$plane, thus mimicking the effect of a vibrating ribbon. At the inflow boundary the integral formulation of the characteristic boundary condition [33] was used to prescribe a Blasius boundary layer profile with a Reynolds number, based on displacement thickness, of $Re_{\delta^*} = 273$. At the freestream and outflow boundaries non-reflective characteristic boundary conditions were applied.
For the body-fitted baseline reference case a rectangular Cartesian grid with $1.59172 \times 10^{-3} < x < 0.45598$ and $0.0 < y < 4.70223 \times 10^{-2}$ was employed. In the streamwise direction the 281 grid points were distributed equidistantly with $\Delta x = 1.623 \times 10^{-3}$ over the whole domain. In the wall normal direction the grid spacing stretched from $\Delta y = 3.51 \times 10^{-5}$ at the wall to $\Delta y = 1.644 \times 10^{-3}$ at the freestream boundary. The spanwise direction was discretized with a spectral method using two Fourier modes for a spanwise extent of $\Delta z = 0.0299817$.
In the validation case where the BDIM represents the wall boundary condition, 20 grid points were mirrored in the wall normal direction. The void below the original position of the wall was initialized with zero velocity and uniform density and temperature. The smoothing region half-width ϵ in units of wall-normal grid spacing in the simulations was $\epsilon = 2.0\Delta y$.

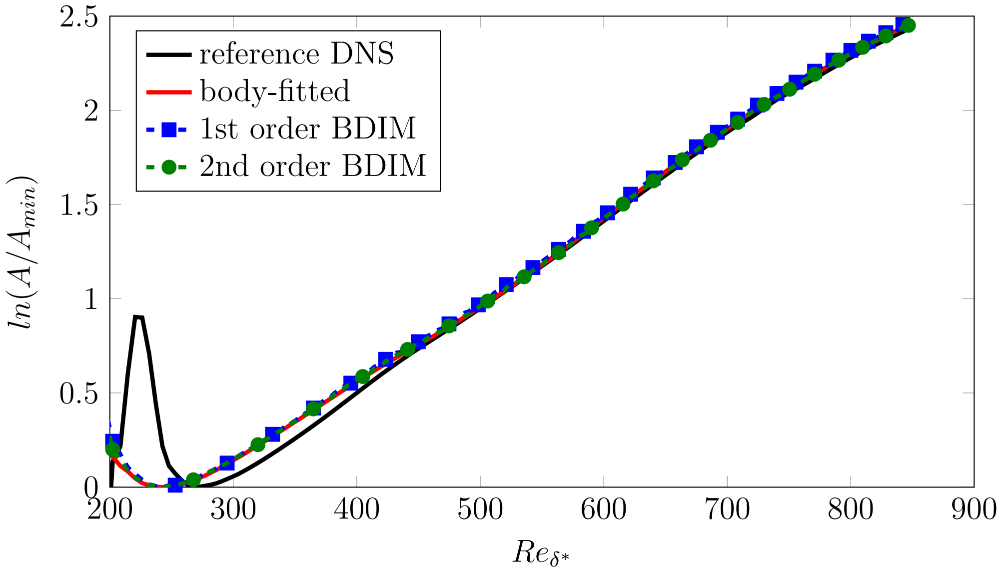

Figure 7: Amplitude of streamwise velocity disturbance as a function of the streamwise position comparing data from [49] with simulations using the BDIM and body-fitted boundary conditions.

3.4.2. Results - Accuracy

After the initial transient instantaneous snapshots of the flow field were gathered for two forcing cycles. From the temporal Fourier transform of the streamwise velocity component the maximum amplitude across the boundary layer was determined as a function of x and then normalized by the lowest amplitude of all streamwise positions during post-processing. Figure 7 compares the results obtained with the BDIM to represent the wall with data using body-fitted boundary conditions with the same code and a reference DNS [49]. It can be noted that there are slight differences between the reference [49] and the body-fitted case in the region of the onset of the instability growth. These can be explained by the fact that the forcing was introduced differently in both cases. Overall it can be appreciated that both the first and second order BDIM reproduce the growth rates very accurately, but the second order BDIM is slightly closer to the reference.

In addition to the instability growth rate, the fluctuation amplitudes of the streamwise velocity u, the density ρ and the temperature T are evaluated in figure 8 as a function of the normalized wall distance at $Re_{\delta^*} = 700$. The amplitudes are normalized by the maximum velocity amplitude. The velocity

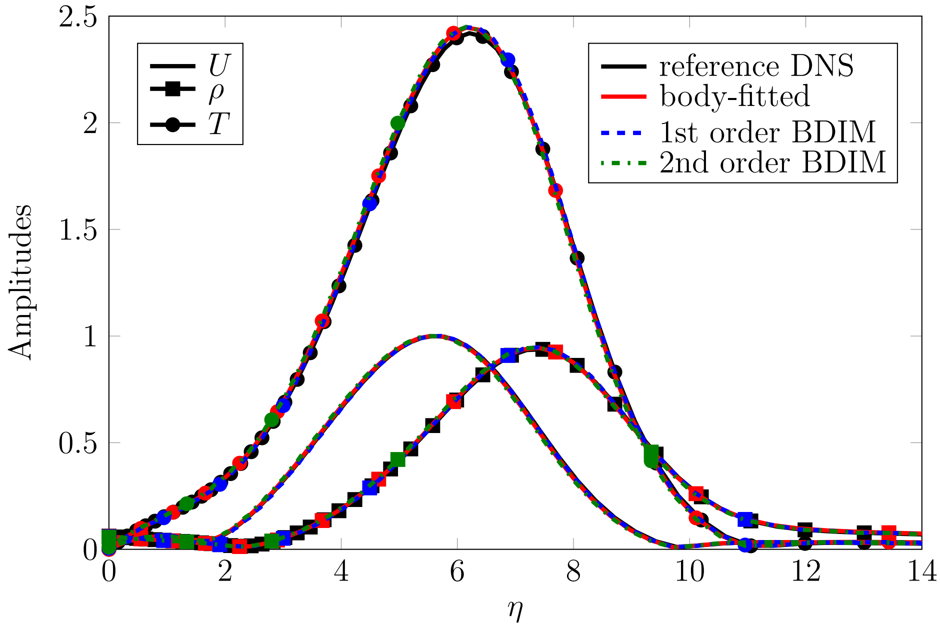

Figure 8: Amplitude distribution of perturbations of streamwise velocity U, density ρ and temperature T in the wall-normal direction at $Re_{\delta^*} = 700$ from the simulations using the BDIM in comparison to simulations with body-fitted boundary conditions and to the results from Husmeier et al. [49]. The wall normal distance y is represented with the similarity variable $\eta = y\sqrt{U/(\nu x)}$, where U is the streamwise velocity component, ν the viscosity and x the streamwise position. All amplitudes are normalized by the maximum of the velocity amplitude.

amplitude profile proves that the very good agreement between the BDIM and the references is not limited to the maximum amplitude of the velocity fluctuations as presented before. It also matches the shape of the profile along the wall normal direction perfectly. Furthermore the fluctuations of the thermodynamic quantities density ρ and temperature T are computed very accurately. In addition, the normalization that was chosen shows that density fluctuations are almost as high as the velocity fluctuations and the temperature fluctuations are a factor of roughly 2.4 higher that the velocity fluctuations, thus underlining the importance of a good representation of the near wall thermodynamic quantities. Computing these quantities accurately even for low energies is crucial for direct noise computations.

Overall the results show that the BDIM is capable of accurately rep-

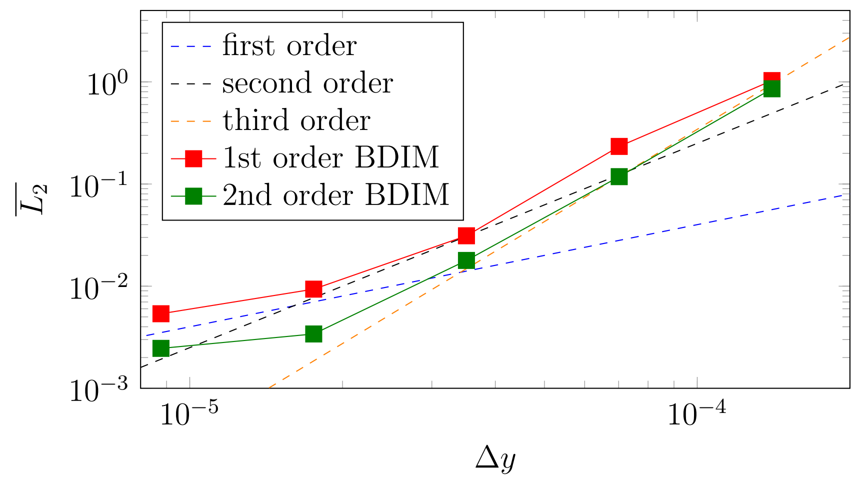

Figure 9: L_2 convergence of the instability growth rates comparing the first and second order BDIM. A first, second and third order slope are plotted as reference.

resenting highly sensitive instability growth adjacent to a wall in a three dimensional compressible flow.

3.4.3. Results - Convergence

A study with 4 additional resolution levels all together spanning a factor of 16 change in resolution was carried out in order to establish convergence of the instability growth rate for this supersonic case. The results are compared employing the L_2 norm of the disturbance amplitude in the streamwise extent $300 < Re_{\delta^*} < 800$ relative to the body-fitted reference in Figure 9. The first order BDIM yields a convergence rate that varies between an order of 1.5 and 3 and tails off at the highest resolution. The second order BDIM shows a constant convergence rate that is estimated to be $2.5 - 3$. It also shows the tail-off at the highest resolution. Overall the error level is lower than in the first order case. From visual inspection of the instantaneous flow field the tail-off is most likely due to a shock downstream of the inflow.

4. Validation for aeroacoustic problems

A great advantage of compressible direct numerical simulations is that the generation of flow noise can be investigated without any further modelling as the relevant physical mechanisms are incorporated in the governing equations, i.e. the hydrodynamic and acoustic field are solved simultaneously.

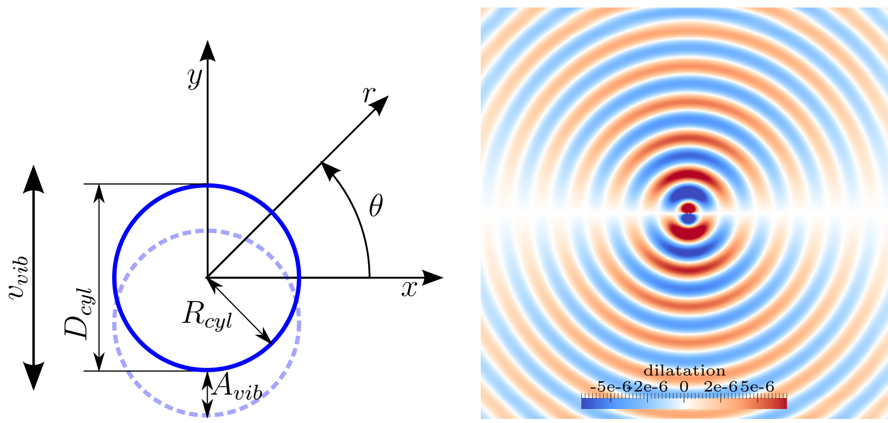

(a) Sketch of the oscillating cylinder.

(b) Instantaneous dilatation contours visualizing the acoustic field radiated from the vibrating cylinder.

Figure 10: Introduction of the nomenclature for the physical problem and instantaneous visualization of the acoustic field.

The use of the BDIM in such simulations enables the consideration of noise generation by flow interaction with moving objects or bodies with complex shapes. The following section validates the BDIM for the use in aeroacoustic simulations and considers the noise radiation from a moving body in a medium at rest and trailing-edge noise from an airfoil.

4.1. Noise radiation from transversely oscillating cylinder

This section considers the noise radiation from a transversely oscillating cylinder. The cylinder is assumed to have an infinite extension in the spanwise direction and can therefore be simplified to a two dimensional problem. The focus of this case is purely on the noise radiation from a moving body and therefore the surrounding medium of the cylinder is assumed to be at rest.

4.1.1. Osciallting cylinder - Numerical setup

The cylinder's diameter D_{cyl} was set to unity and the vibration amplitude A_{vib} was 5% of the diameter. The vibration frequency was $f_{vib} = 0.03$ which results in an amplitude for the vibration velocity of $|v_{vib}| \approx 9.42 \times 10^{-3}$. With a Mach number of $M = 1$ these parameters result in an acoustic wave length of $\lambda_a = M/f_{vib} = 33.3D_{cyl}$. The nomenclature and definition of the parameters is also visualized in figure 10a. The cylinder was discretized with 160 equispaced grid points per diameter and surrounded by another $1.25d_{cyl}$ of equispaced grid with the same resolution in each direction. For the transition between the near and the far-field the grid was stretched over 200 grid points to a resolution of 20 grid points per acoustic wave length. The far field of the domain with that resolution covers $6\lambda_a$ approximately. Since the oscillating cylinder is the only noise source and its strength is rather low even minor reflections from the domain boundaries can contaminate the acoustic field. Therefore the outgoing acoustic waves were damped with strong stretching towards the boundaries over an additional 40 grid points in conjunction with the non-reflective boundary conditions.

4.1.2. Osciallting cylinder - results

The analytical solution for the pressure fluctuations p_{rms} of this radiation problem is

$$p_{rms} = \frac{1}{\sqrt{2}} \left| -j\rho_0 v_{vib} cos(\theta) \frac{H_1^{(2)}(k_a r)}{M\, H_1^{(2)'}(k_a R_{cyl})} e^{j2\pi f_{vib} t} \right| \quad , \tag{27}$$

where $H_1^{(2)}$ is a Hankel function of the second kind and first order and $H_1^{(2)'}$ its derivative with the wave number $k_a = 1/\lambda_a$ as part of its argument. Furthermore ρ_0 is the mean density of the medium at rest [50]. The near field approximation can be expressed by

$$p_{rms} = \frac{1}{\sqrt{2}} \left| -j2\pi f_{vib} \rho_0 v_{vib} R_{cyl}^2 M^2 \frac{1}{r} \right| \quad , \tag{28}$$

and the far field approximation is

$$p_{rms} = \frac{1}{\sqrt{2}} \left| 2\pi^2 f_{vib}^{1.5} \rho_0 R_{cyl}^2 v_{vib} M^{1.5} \frac{1}{\sqrt{r}} \right| \quad . \tag{29}$$

Figure 10b presents the dilatation contours at an arbitrary instance of time from the simulation with the first order BDIM. The dilatation contours show the expected dipole like radiation pattern with no signs of any spu-

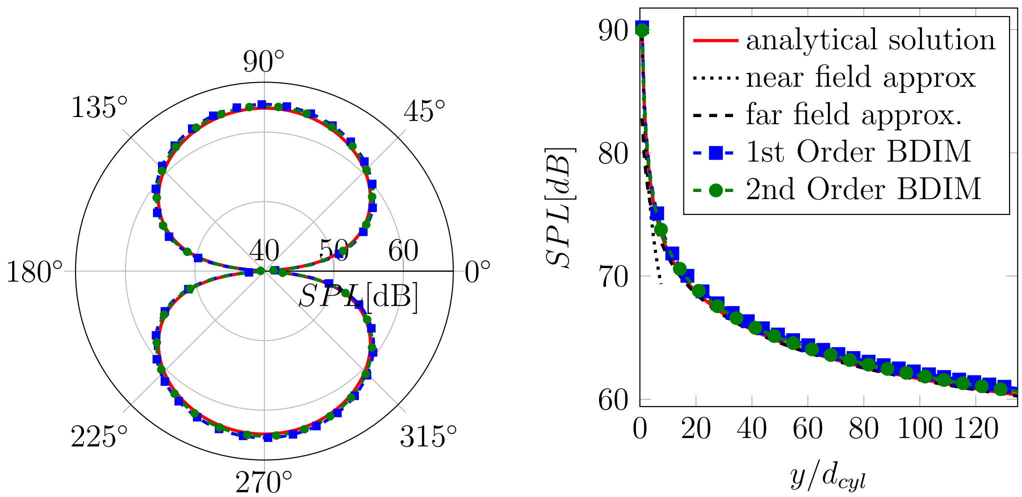

(a) Directivity of noise radiated from the cylinder at a radial distance of $r = 2\lambda_a$ or $r = 132D_{cyl}$. For the legend refer to the neighboring figure.

(b) Pressure fluctuations from the analytical prediction and the simulation results.

Figure 11: Quantitative validation comparing the data from the simulation to the analytical reference.

rious oscillations from either the domain boundaries or the BDIM. This is confirmed by the averaged directivity of the radiated sound pressure levels (SPL) in Figure 11a. The data is extracted from the acoustic far-field at a radial distance of $r = 2\lambda_a$. It can be appreciated that the shape of the directivity pattern simulated by the BDIM is in excellent agreement with the analytical reference. The amplitudes of the two simulations employing the BDIM agree reasonably well with the reference but are slightly overestimated at this resolution level of $\Delta x = \Delta y = D_{cyl}/160$.

Figure 11b compares the SPL as a function of the radial distance of the two simulations with the analytical solution. The data was extracted along the radial direction aligned with the cylinder's motion. The findings from the SPL directivity are confirmed in that the simulations employing the BDIM slightly overestimate the SPL by a constant value. It is apparent that the second Order BDIM agrees better with the reference than the first order approach. Table 2 compares the averaged deviation from the analytical reference along the main radiation direction for the first and second order BDIM for different resolution levels. The deviation from the analytical solution is a

N_{pts}/D_{cyl}	$A_{vib}/\Delta x$	1st Ord BDIM ΔSPL[dB]	2nd Ord BDIM ΔSPL[dB]
20	1	2.91	1.64
40	2	1.64	0.88
80	4	0.92	0.48
160	8	0.53	0.29
320	16	0.34	0.21
640	32	0.25	0.18

Table 2: Summary of deviation from the analytical reference for different resolution levels using the first and second order BDIM .

factor of 1.39 to 1.92 higher when the first order BDIM is employed compared to the second order. The formal order of convergence of the data presented in table 2 is visualized in Figure 12. It is obvious that the first and second order BDIM converge with the same rate of approximately one. The major difference between the two is the level of the deviation, as discussed before. The fact that both cases yield the same rate of convergence is not surprising. As shown with the results from the turbulent boundary layer in Figure 4, the main effect of the second order correction is the improved representation of the wall velocity gradient in the wall bounded shear flow. In the current case considering an oscillating cylinder in a medium at rest the shear is very small.

For the highest resolution a tail off can be observed for both cases. This is not the case when the data is referenced to the highest resolution case and not the analytical reference. This indicates that the tail off is not due to boundary conditions but that the simulation converges to a different solution as is also suggested by the constant offset found in the previous discussion. The most likely reason for that is the assumption of an inviscid fluid in the derivation of the analytical solution. However, the simulations do have a finite viscosity. An additional test simulation showed that when the viscosity is increased by two orders or magnitude the deviation between the analytical solution and the simulated result decreases to $\Delta SPL = 0.47$dB on the $N_{pts}/D_{cyl} = 80$ grid using the second order framework. When viscosity was reduced by two orders of magnitude this deviation grew to $\Delta SPL = 1.72$dB on the same grid and with the same method. The action of viscosity adds

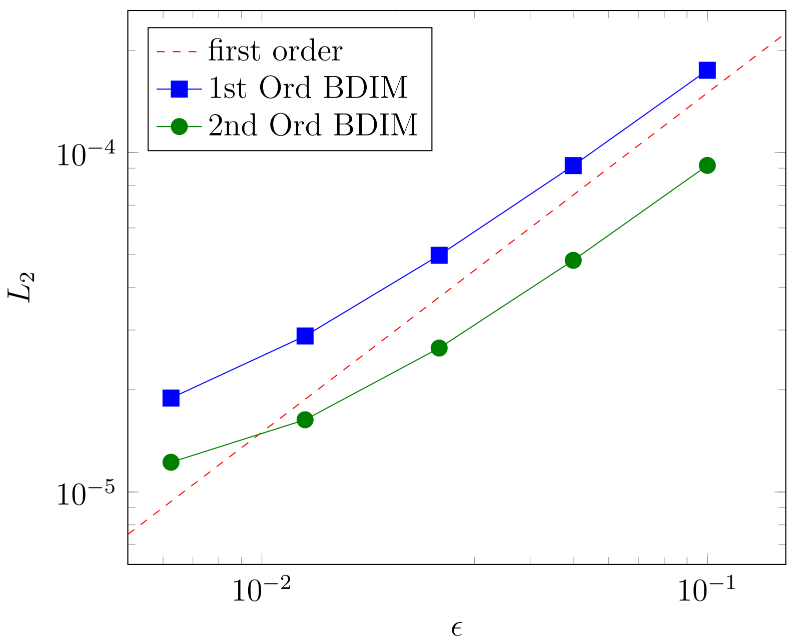

Figure 12: Convergence of the pressure fluctuations relative to the analytical reference over the kernel half-width ϵ for the first and the second order BDIM.

an additional component of fluid acceleration tangential to the translation direction.

In summary the overall agreement with the analytical reference is excellent considering the very low energies that are involved in this acoustic test case. This validation case demonstrates that the BDIM is an appropriate method to perform high-fidelity simulations featuring noise radiation from moving bodies.

4.2. Noise radiation from an airfoil with a trailing-edge extension

~~This paragraph considers~~ trailing-edge noise from a trailing-edge extension of an airfoil at angle of attack. In this validation case the aeroacoustic noise generation is caused by the interaction of a stationary body with the unsteady flow around it. The noise radiation from the trailing-edge will be the strongest source of noise in this case as the interaction of pressure fluctuations in the flow with the rigid trailing-edge increases the efficiency of the radiation process.

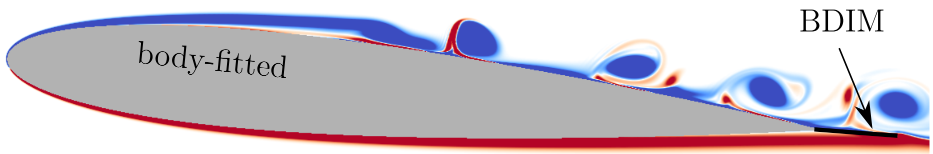

(a) Snapshot of the spanwise vorticity field indicating where the BDIM is employed and the separation on the suction side.

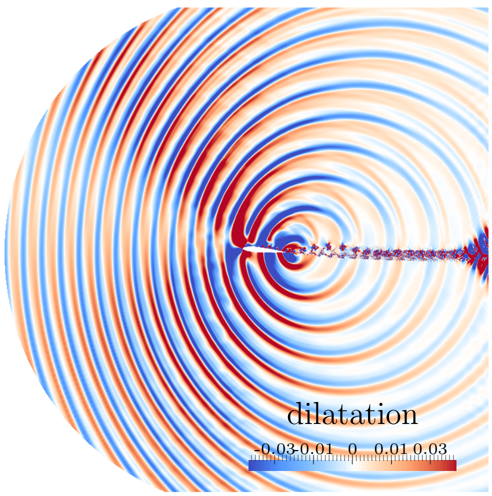

(b) Dilatation contours of a simulation where the 1st order BDIM is employed to represent the the airfoil's extension.

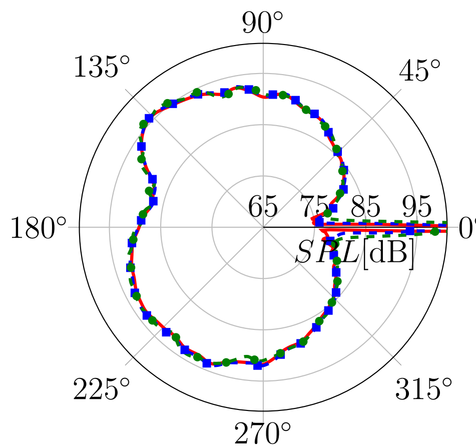

(c) Noise levels at a radial distance of $r = 4$ chord lengths comparing simulation results with body-fitted boundary conditions(——) and the first (- ■ -) and second (- ● -) order BDIM.

Figure 13: Body-fitted airfoil simulation where the extension is represented by the BDIM.

4.2.1. Airfoil trailing-edge noise - Numerical setup

The flow parameters of this case are the chord based Reynolds number $Re_c = 5 \times 10^4$, Mach number $M = 0.4$ and angle of attack $AoA = 5°$. At these flow conditions the flow separates on the suction side and forms a laminar separation bubble as can be seen in the spanwise vorticity contours presented in figure 13a. The computational grid was derived from the grid G3 in Jones et al. [51]. In order to optimize the resolution close to the airfoil surface and reduce numerical cost the airfoil body is represented by a body conforming grid and body-fitted boundary conditions. As indicated in figure 13a the trailing-edge extension was represented by the BDIM. This hybrid approach reduces the computational cost significantly but leaves the flexibility to change the shape of the extension or make it an actuated moving control surface.

4.2.2. Airfoil trailing-edge noise - Results

The acoustic field of this case is visualized with contours of dilatation in figure 13b. It can be seen that the noise originates from the trailing-edge of the extension and travels predominantly in the upstream direction. The acoustic field is very clean and shows no signs of spurious oscillations from the domain boundaries or the BDIM.

Figure 13c compares the noise directivity when the flat plate extension is represented by either body-fitted boundary conditions and by the BDIM. This plot shows excellent agreement between the two cases employing the BDIM and the body-fitted boundary conditions for the noise level as well as for the directivity shape. This demonstrates that the first and second order BDIM are able to represent the acoustic scattering of pressure disturbances from a trailing-edge accurately.

5. Conclusion

The compressible extension of the Boundary Data Immersion Method originally developed for incompressible flows [11] has been introduced. The compressible formulation uses the BDIM meta equation to map the velocity and temperature fields between a solid body and a fluid subdomain. For certain applications such as the simulation of bluff bodies the proposed mapping of the continuity equation as an interface condition between fluid and solid can enhance robustness of the simulation.

A thorough validation of the novel compressible BDIM framework showed that the second order extension increases accuracy of the simulations compared to the first order approach. In particular the discontinuity of the velocity gradient at the wall is modelled much more accurately. This ~~could be~~ shown for the very challenging case of a fully turbulent boundary layer where the discontinuity of the velocity gradient is relatively high and a broad range of scales in time and space is present in the flow.

The case of a transversely oscillating cylinder in a medium at rest showed that the BDIM is able to predict the noise radiation from a moving body with high accuracy. Furthermore flow induced noise generated by the interaction of a solid body with unsteady fluid flow can be modelled accurately with the BDIM. To the authors' knowledge this is the first virtual boundary method that has been validated for direct noise simulations considering moving bodies.

There is no penalty in allowable time step compared to body-fitted simulations when using the BDIM. In all cases considered the second order correction reduced the solution error and improved the convergence rate. Hence the BDIM for compressible flows offers a computationally efficient yet accurate approach to represent stationary or moving bodies in high-fidelity numerical simulations with application to aeroacoustics. The method has already been employed successfully for fluid-structure interaction problems [52]. We also envision it to be appropriate for aero-vibro-acoustic studies and other applications that require accurate representation of arbitrary moving boundaries.

Acknowledgement

The first author acknowledges the faculty for Engineering and the Environment of the University of Southampton for funding his PhD. Furthermore this work used the ARCHER UK National Supercomputing Service (http://www.archer.ac.uk) for which computational time was provided through the UK turbulence consortium, EPSRC grant number EP/L000261/1 and is gratefully acknowledged.

AppendixA. Weighting functions at the intersection of two planes

In Section 2, kernel moments are analytically evaluated in order to accurately immerse the boundary data from the solid mechanical system onto the fluid mechanical equations of motion. In the appendix, the case of a geometry with sharp corners (which requires special care) is locally treated as the intersection of two component planar geometries.

First we use Eq 6a to determine the moment at point $\vec{x}$ of each of the component planes a and b, and call them $\mu_{0,a}$, $\mu_{0,b}$. We name these planes such that $\mu_{0,a} \leq \mu_{0,b}$, ie $\vec{x}$ is further into the fluid relative to a. In the case that x is not near the intersection, the moment of the shape c defined as the intersection of a and b is simply the moment of a,

$$\mu_{0,c} = \mu_{0,a} \tag{A.1}$$

However, when $\vec{x}$ is in the smoothing region of both a and b, such that $0 < \mu_{0,a} \leq \mu_{0,b} < 1$, then both planes contribute to the compound moment. An approximate value for the compound moment in this case is

$$\mu_{0,c} = \mu_{0,a}\mu_{0,b}^{\log_2 \frac{\pi}{\theta}} \tag{A.2}$$

subject to the bound

$$\mu_{0,c} \geq \max(0, \mu_{0,a} + \mu_{0,b} - 1) \tag{A.3}$$

We see that the angle θ between a and b determines how heavily $\mu_{0,b}$ influences the compound moment. For $\theta = \pi$, the compound shape is flat and there is no change to Eq A.1. For $\theta < \pi$, the shape is a sharp corner, and the moment decreases sharply as you approach the intersection of the two planes. The bound ensures that the compound moment is still accurate for very small angles when the kernel regions of the two planes do not overlap.

Once this moment is established, it implicitly defines the effective distance d_c and normal $\hat{n}_c$ of the compound shape. If $\mu_{0,c}$ is given by Eq A.1 then $d_c = d_a$ and $\hat{n}_c = \hat{n}_a$. Otherwise, the distance d_c is found by inverting Eq 6a. Note that the bounds on $\mu_{0,c}$ ensure we only need the first line of Eq 6a. Let us call the inverse of the Eq 6a h, ie

$$d(\vec{x}) = h(\mu_0(\vec{x}))$$

Then $d_c = h(\mu_{0,c})$ is used in Eq 16b to find the effective first moment $\mu_{1,c}$ without issue.

The normal $\hat{n}$ is defined as

$$\hat{n}(\vec{x}) = \vec{\nabla} d(\vec{x}) = h'(\mu_0)\vec{\nabla}\mu_0(\vec{x}) \tag{A.4}$$

where

$$h' = \frac{\partial h}{\partial \mu_0}$$

and we note that h' only scales the magnitude not the direction of the normal. First, let's assume that the lower bound Eq A.3 is active, then the normal is proportional to

$$\hat{n}_c \propto \vec{\nabla}\mu_{0,a} + \vec{\nabla}\mu_{0,b} = \frac{\hat{n}_a}{h'(\mu_{0,a})} + \frac{\hat{n}_b}{h'(\mu_{0,b})}$$

where Eq A.4 is used to substitute the normal for each component. We see the effective normal is a weighted sum of the component normals.

Next, using Eq A.2, applying the chain rule, and substituting the normals for each component as before gives

$$\hat{n}_c \propto \frac{1}{\mu_{0,a}} \frac{\hat{n}_a}{h'(\mu_{0,a})} + \frac{\log_2(\frac{\pi}{\theta})}{\mu_{0,b}} \frac{\hat{n}_b}{h'(\mu_{0,b})}$$

where again we see that the angle θ determines the relative influence of plane b.

References

[1] R. Mittal, G. Iaccarino, Immersed boundary methods, Annual Review of Fluid Mechanics 37 (2005) 239–261.

[2] H. Udaykumar, R. Mittal, P. Rampunggoon, A. Khanna, A Sharp Interface Cartesian Grid Method for Simulating Flows with Complex Moving Boundaries, Journal of Computational Physics 174 (2001) 345–380. doi:10.1006/jcph.2001.6916.

[3] J. Yang, E. Balaras, An embedded-boundary formulation for large-eddy simulation of turbulent flows interacting with moving boundaries, Journal of Computational Physics 215 (2006) 12–40. doi:10.1016/j.jcp.2005.10.035.

[4] R. Mittal, H. Dong, M. Bozkurttas, F. Najjar, A. Vargas, A. von Loebbecke, A versatile sharp interface immersed boundary method for incompressible flows with complex boundaries, Journal of Computational Physics 227 (2008) 4825–4852. doi:10.1016/j.jcp.2008.01.028.

[5] J. Seo, R. Mittal, A Sharp-Interface Immersed Boundary Method with Improved Mass Conservation and Reduced Spurious Pressure Oscillations, Journal of Computational Physics 230 (2011) 7347–7363. doi:10.1016/j.jcp.2011.06.003.

[6] H. Luo, H. Dai, P. Ferreira de Sousa, B. Yin, On the numerical oscillation of the direct-forcing immersed-boundary method for moving boundaries, Computers & Fluids 56 (2012) 61–76. doi:10.1016/j.compfluid.2011.11.015.

[7] C. Liu, C. Hu, An efficient immersed boundary treatment for complex moving object, Journal of Computational Physics 274 (2014) 654–680. doi:10.1016/j.jcp.2014.06.042.

[8] M. Uhlmann, An immersed boundary method with direct forcing for the simulation of particulate flows, Journal of Computational Physics 209 (2005) 448–476. doi:10.1016/j.jcp.2005.03.017.

[9] M. Vanella, E. Balaras, A moving-least-squares reconstruction for embedded-boundary formulations, Journal of Computational Physics 228 (2009) 6617–6628. doi:10.1016/j.jcp.2009.06.003.

[10] A. Pinelli, I. Z. Naqavi, U. Piomelli, J. Favier, Immersed-boundary methods for general finite-difference and finite-volume Navier-Stokes solvers, Journal of Computational Physics 229 (2010) 9073–9091. doi:10.1016/j.jcp.2010.08.021.
URL `http://dx.doi.org/10.1016/j.jcp.2010.08.021`

[11] A. Maertens, G. Weymouth, Accurate Cartesian-grid simulations of near-body flows at intermediate Reynolds numbers, Computer Methods in Applied Mechanics and Engineeringdoi:10.1016/j.cma.2014.09.007.

[12] W. P. Breugem, A second-order accurate immersed boundary method for fully resolved simulations of particle-laden flows, Journal of Computational Physics 231 (2012) 4469–4498. doi:10.1016/j.jcp.2012.02.026.
URL `http://dx.doi.org/10.1016/j.jcp.2012.02.026`

[13] G. Weymouth, D. Yue, Boundary data immersion method for Cartesian-grid simulations of fluid-body interaction problems, Journal of Computational Physics 230 (2011) 6233–6247. doi:10.1016/j.jcp.2011.04.022.

[14] A. Chaudhuri, A. Hadjadj, A. Chinnayya, On the use of immersed boundary methods for shock/obstacle interactions, Journal of Computational Physics 230 (2011) 1731–1748. doi:10.1016/j.jcp.2010.11.016.

[15] P. Tran, F. Plourde, Computing compressible internal flows by means of an Immersed Boundary Method, Computers & Fluids 97 (2014) 21–30. doi:10.1016/j.compfluid.2014.03.009.

[16] D. Casalino, P. di Francescantonio, Y. Druon, GFD Predictions of Fan Noise Propagation, in: 10th AIAA/CEAS Aeroacoustics Conference, AIAA Paper 2004-2989, 2004.

[17] R. Arina, An Immersed Boundary Method for Aeroacoustics Problems, in: 14th AIAA/CEAS Aeroacoustics Conference, AIAA Paper 2008-3003, 2008.

[18] M. Cand, A. Sayma, M. Imregun, 10th AIAA/CEAS Aeroacoustics Conference, in: 10th AIAA/CEAS Aeroacoustics Conference, AIAA Paper 2004-2816, 2004.

[19] M. Liu, K. Wu, Aerodynamic noise propagation simulation using immersed boundary method and finite volume optimized prefactored compact scheme, Journal of Thermal Science 17 (4) (2008) 361–367. doi:10.1007/s11630-008-0361-x.

[20] J. H. Seo, R. Mittal, A High-Order Immersed Boundary Method for Acoustic Wave Scattering and Low-Mach Number Flow-Induced Sound in Complex Geometries., Journal of Computational Physics 230 (4) (2011) 1000–1019. doi:10.1016/j.jcp.2010.10.017.

[21] F. Margnat, Hybrid prediction of the aerodynamic noise radiated by a rectangular cylinder at incidence, Computers & Fluids 109 (2015) 13–26. doi:10.1016/j.compfluid.2014.12.006.

[22] D. Goldstein, G. Handler, L. Sirovich, Modeling a no-slip flow boundary with an external force field, Journal of Computational Physics 105 (1993) 354–366.

[23] P. De Palma, M. de Tullio, G. Pascazio, M. Napolitano, An immersed-boundary method for compressible viscous flows, Computers & Fluids 35 (2006) 693–702. doi:10.1016/j.compfluid.2006.01.004.

[24] M. de Tullio, P. De Palma, G. Iaccarino, G. Pascazio, M. Napolitano, An immersed boundary method for compressible flows using local grid refinement, Journal of Computational Physics 225 (2007) 2098–2117. doi:10.1016/j.jcp.2007.03.008.

[25] R. Ghias, R. Mittal, H. Dong, A sharp interface immersed boundary method for compressible viscous flows, Journal of Computational Physics 225 (2007) 528–553. doi:10.1016/j.jcp.2006.12.007.

[26] Q. Liu, O. Vasilyev, A Brinkman penalization method for compressible flows in complex geometries, Journal of Computational Physics 227 (2007) 946–966. doi:10.1016/j.jcp.2007.07.037.

[27] R. Sandberg, L. Jones, Direct numerical simulations of low Reynolds number flow over airfoils with trailing-edge serrations, Journal of Sound and Vibration 330 (2011) 3818–3831.

[28] O. Hu, N. Zhao, J. Liu, A Ghost Cell Method for Turbulent Compressible Viscous Flows on Adaptive Cartesian Grids, Procedia Engineering 67 (2013) 241–249. doi:10.1016/j.proeng.2013.12.023.

[29] M. Carpenter, J. Norstrom, D. Gottlieb, A stable and conservative interface treatment of arbitrary spatial accuracy, Journal of Computational Physics 148 (1999) 341–365.

[30] C. A. Kennedy, M. H. Carpenter, R. M. Lewis, Low-storage, explicit RungeKutta schemes for the compressible NavierStokes equations, Applied Numerical Mathematics 35 (2000) 177–219.

[31] C. A. Kennedy, A. Gruber, Reduced aliasing formulations of the convective terms within the Navier-Stokes equations for a compressible fluid, Journal of Computational Physics 227 (3) (2008) 1676–1700. doi:10.1016/j.jcp.2007.09.020.

[32] C. Bogey, N. de Cacqueray, C. Bailly, A shock-capturing methodology based on adaptative spatial filtering for high-order non-linear computations, Journal of Computational Physics 228 (5) (2009) 1447–1465. doi:10.1016/j.jcp.2008.10.042.

[33] L. E. Jones, Numerical studies of the flow around an airfoil at low Reynolds number, Ph.D. thesis, School of Engineering Sciences University of Southampton (2008).

[34] R. Sandberg, N. Sandham, Nonreflecting zonal characteristic boundary condition for direct numerical simulation of aerodynamic sound, AIAA Journal 44 (2) (2006) 402–405.

[35] J. Park, K. Kwon, H. Choi, Numerical solutions of flow past a circular cylinder at Reynolds numbers up to 160, KSME International Journal 12 (6) (1998) 1200–1205. doi:10.1007/BF02942594.

[36] R. Henderson, Details of the drag curve near the onset of vortex shedding, Physics of Fluids 7 (1995) 2102–2104. doi:10.1063/1.868459.

[37] H. Zhang, U. Fey, B. Noack, M. König, H. Eckelmann, H.-q. Zhang, U. Fey, B. R. Noack, On the transition of the cylinder wake, Physics of Fluids 7 (1995) 779–794. doi:10.1063/1.868601.

[38] J.-I. Choi, R. C. Oberoi, J. R. Edwards, J. A. Rosati, An immersed boundary method for complex incompressible flows, Journal of Computational Physics 224 (2007) 757–784. doi:10.1016/j.jcp.2006.10.032.

[39] P. H. Chiu, R. K. Lin, T. W. H. Sheu, A differentially interpolated direct forcing immersed boundary method for predicting incompressible NavierStokes equations in time-varying complex geometries, Journal of Computational Physics 229 (2010) 4476–4500. doi:10.1016/j.jcp.2010.02.013.

[40] D. Russell, Z. J. Wang, A Cartesian grid method for modeling multiple moving objects in 2D incompressible viscous flow, Journal of Computational Physics 191 (2003) 177–205. doi:10.1016/S0021-9991(03)00310-3.

[41] C. Norberg, An experimental investigation of the flow around a circular cylinder: influence of aspect ratio, Journal of Fluid Mechanics 258 (1994) 287–316. doi:10.1017/S0022112094003332.

[42] D. J. Tritton, Experiments on the flow past a circular cylinder at low Reynolds numbers, Journal of Fluid Mechanics 6 (1959) 547–567. doi:10.1017/S0022112059000829.

[43] E. Saiki, S. Biringen, Numerical simulation of a cylinder in uniform flow: application of a virtual boundary method, Journal of Computational Physics 123 (1996) 450–465.

[44] M. Klein, A. Sadiki, J. Janicka, A digital filter based generation of inflow data for spatially developing direct numerical or large eddy simulations, Journal of Computational Physics 186 (2003) 652–665. doi:10.1016/S0021-9991(03)00090-1.

[45] E. Touber, N. Sandham, Large-eddy simulation of low-frequency unsteadiness in a turbulent shock-induced separation bubble, Theoretical and Computational Fluid Dynamics 23 (2009) 79–107. doi:10.1007/s00162-009-0103-z.

[46] P. Schlatter, R. Örlü, Assessment of direct numerical simulation data of turbulent boundary layers, Journal of Fluid Mechanics 659 (2010) 116–126. doi:10.1017/S0022112010003113.

[47] P. Schlatter, R. Örlü, Turbulent boundary layers at moderate Reynolds numbers: inflow length and tripping effects, Journal of Fluid Mechanics 710 (2012) 5–34. doi:10.1017/jfm.2012.324.

[48] C. Mayer, D. von Terzi, H. Fasel, Direct numerical simulation of complete transition to turbulence via oblique breakdown at Mach 3, Journal of Fluid Mechanics 674 (2011) 5–42.

[49] F. Husmeier, C. Mayer, H. Fasel, Investigation of Transition of Supersonic Boundary Layers at Mach 3 Using DNS, in: 43th AIAA Aerospace Sciences Meeting and Exhibit, 2005.

[50] D. Blackstock, Fundamentals of Physical Acoustics, John Wiley & Sons, 2000.

[51] L. E. Jones, R. D. Sandberg, N. D. Sandham, Direct numerical simulations of forced and unforced separation bubbles on an airfoil at incidence, Journal of Fluid Mechanics 602 (2008) 175–207.

[52] S. Serrano Galliano, R. Sandberg, Effect of the leading and trailing edge geometry on the fluid-structural coupling of membrane aerofoils, in: 2016 AIAA SciTech, AIAA Paper 2016-0853, 2016.